

Chapter 8

Analysis of Quasar Spectra

8.1 Low Resolution Spectra

Low resolution spectra, those having $R \leq 3000$, are useful for survey work (see Chapter 9). A substantial fraction of the absorption lines will be unresolved, meaning that their line widths will be the width of the instrumental spread function (§ 7.1.6). As such, these spectra are most useful for scientific objectives such as line counting and evolution studies. In this chapter, methods for obtaining objective accounting of features in the low resolution spectra are addressed.

8.1.1 Objective Feature Finding

Absorption (and emission) features must be statistically significant and should always be based upon an objective algorithm. Ensuring statistical significance and objectivity requires proper and careful accounting of the errors for the measured counts in each pixel. Thus, the uncertainty spectrum, σ_{I_λ} , plays a critical role in the objective definition. Before proceeding with feature identification, it should be verified that the uncertainty spectrum is a sound representation of the fluctuations in the data.

8.1.1.1 Aperture Method

Absorption and emission features in the spectra can be identified using the “aperture” method, which is described in some detail by ?. This technique

is *not* optimal, however, for weak unresolved lines, which are best detected using the instrumental profile weighting technique (discussed in § 8.1.1.2).

Once an objective line list is constructed, the observed equivalent widths and uncertainties can be computed. It is best to use the “equivalent width” of each pixel, w_j , where j represents the pixel index, and the uncertainty, σ_{w_j} , to locate pixels that depart significantly from the surrounding continuum. Thus, one needs to compute an “equivalent width spectrum” from the data. The observed “equivalent width” of a single pixel is defined as

$$w_j = \left(\frac{I_j}{I_j^c} - 1 \right) \Delta\lambda_j, \quad (8.1)$$

where I_j is the flux in pixel j , I_j^c is its fitted continuum level, and $\Delta\lambda_j = (\lambda_{j-1} - \lambda_{j+1})/2$ is the wavelength interval spanned by the pixel. Note that w_j is defined such that $w_j < 0$ for absorption and $w_j > 0$ for emission. The variance in w_j is given by

$$\sigma_{w_j}^2 = \left(\frac{\partial w_j}{\partial I_j} \right)^2 \sigma_{I_j}^2 + \left(\frac{\partial w_j}{\partial I_j^c} \right)^2 \sigma_{I_j^c}^2 = \Delta\lambda_j \left[\left(\frac{\sigma_{I_j}}{I_j^c} \right)^2 + \left(\frac{I_j \sigma_{I_j^c}}{[I_j^c]^2} \right)^2 \right], \quad (8.2)$$

where the σ_{I_j} are the 1σ uncertainties in the I_j resulting from data reduction and calibration sources and due to Poisson noise in the quasar flux and the sky. We have included uncertainty due to the continuum placement in the above treatment.

Once these quantities are computed, a pixel is considered to depart from the continuum by N_σ , when the condition

$$r_j = \left| \frac{w_j}{\sigma_{w_j}} \right| \geq N_\sigma, \quad (8.3)$$

is met, where N_σ is usually taken to be in the range 3–5. The absolute values are required due to the formalism of defining “absorption pixels” to have $w_j < 0$. True features will have a few to several pixels with $r_j > N_\sigma$; the number should be greater than or equal to the number of pixels per resolution element.

The “aperture” of each feature, is defined by the first occurrence of $|w_j| \leq \sigma_{w_j}$ as the local region of the spectrum satisfying Eq. 8.3 is scanned toward the blue, yielding the lower limit pixel, j_- , and toward the red, yielding the upper limit pixel, j_+ . The observed equivalent width, W_i , uncertainty, σ_{W_i} , and significance level, SL_i , of the i th feature are then computed from

$$W_i = \sum_{j_-}^{j_+} w_j, \quad (8.4)$$

$$\sigma_{W_i}^2 = \sum_{j-}^{j+} \sigma_{w_j}^2, \quad (8.5)$$

and,

$$SL_i = \frac{|W_i|}{\sigma_{W_i}} \quad (8.6)$$

respectively. A final filter is then applied to cull the final line list. The criterion is

$$SL_i = \left| \frac{W_i}{\sigma_{W_i}} \right| \geq N_\sigma, \quad (8.7)$$

where, as before, N_σ is usually taken to be in the range 3–5. A drawback of this method is that when multiple individual lines are blended into a single complex feature, the individual lines are not treated separately, only the full feature is measured. Breaking these into their components would require a deblending technique, such as Gaussian fitting (discussed in § 8.1.2). In the absence of deblending, the feature centroid can be found by weighting the wavelength in each pixel by w_j , following

$$\langle \lambda_i \rangle = \frac{\sum_{j-}^{j+} |w_j| \lambda_j}{\sum_{j-}^{j+} |w_j|}. \quad (8.8)$$

8.1.1.2 Optimized Method

The aperture method is not optimized to locate weak unresolved lines in the spectra. In the aperture method, the equivalent width in a pixel, w_j , defined in Eq. 8.1, does not account for the fact that there are contributions from adjacent pixels weighted by the ISF profile. In the core of an unresolved line, this results in an underestimate of w_j due to continuum counts distributed into the line core and wings and due to counts in the line core being distributed outward to the line wings and continuum. With this in mind, ? introduced an optimized method for the purpose of objectively locating weak unresolved absorption (and emission) lines.

For computational purposes, the distribution of counts from a pixel is described by a discrete model, P_i , of the ISF consisting of $M = 2J_0 + 1$ elements, where J_0 is a positive integer equaling twice the number of pixels per resolution element. The pixel indexing of the ISF model is defined to be symmetric with the peak value of P_i at the center pixel, $i = J_0 + 1$. Note that M is an odd integer, providing the discrete model with an equal even

number of pixels either side to the center pixel. To ensure conservation of counts

$$\sum_{i=1}^M P_i = 1, \quad (8.9)$$

where $P_i > 0$ everywhere.

Often, the ISF model is taken to be a discretized Gaussian function with a FWHM given by $\Delta\lambda = \lambda/R$, where R is the spectral resolution. An important point is that the FWHM of the ISF model increases in proportion to λ ; it is not a constant. Defining the ISF centered on pixel j in terms of a Gaussian width,

$$\Delta\sigma_j = \frac{\Delta\lambda_j}{2.35} = \frac{\lambda_j}{2.35R}, \quad (8.10)$$

the discretized ISF can be expressed

$$P_i = C_i \exp \left[- \left(\frac{\lambda_i - \lambda_j}{\Delta\sigma_j} \right)^2 \right], \quad (8.11)$$

with

$$\frac{1}{C_i} = \sum_{i=1}^M \exp \left[- \left(\frac{\lambda_i - \lambda_j}{\Delta\sigma_j} \right)^2 \right], \quad (8.12)$$

where the sum is over the M pixels of the ISF function P_i centered on pixel j .

The optimized value of w_j is obtained by weighting the flux decrement of adjacent pixels by the ISF model,

$$w_j = \frac{\Delta\lambda_j}{P^2} \sum_{i=1}^M P_i D_k, \quad (8.13)$$

where

$$P^2 = \sum_{i=1}^M P_i^2, \quad (8.14)$$

and where the sum is over the index $i = 1, M$, the pixels of the ISF function P_i centered on pixel j . The wavelength interval spanned by the pixel is $\Delta\lambda_j = (\lambda_{j-1} - \lambda_{j+1})/2$, and the “convolution” index is $k = j + (i - 1) + J_0$. The flux decrement being weighted into pixel j from the k th adjacent pixel is

$$D_k = \frac{I_k}{I_k^c} - 1 \quad (8.15)$$

where I_k is the flux in pixel k , and I_k^c is its fitted continuum level. Note that D_k is defined such that $w_j < 0$ for absorption and $w_j > 0$ for emission.

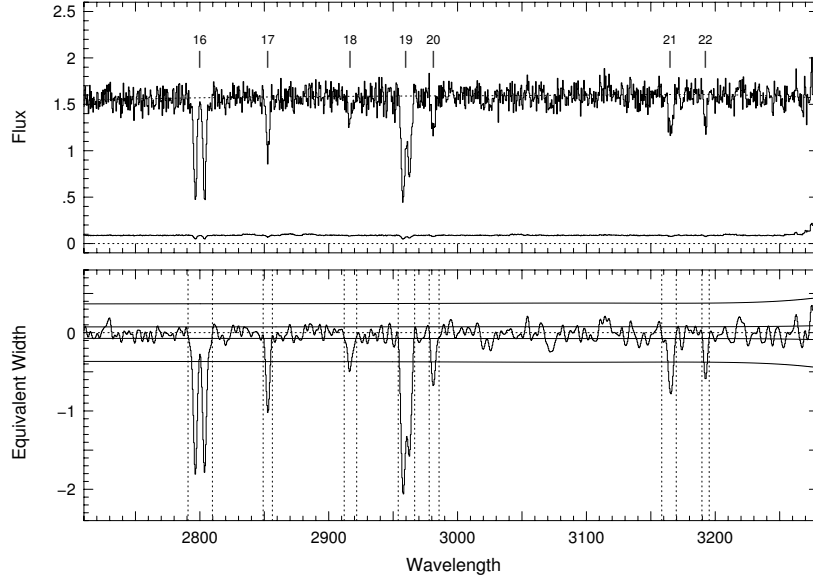


Figure 8.1: — (upper) An example quasar spectrum with objectively found absorption features with $N_\sigma = 5$. Ticks above the continuum identify the centroids of each feature, which can comprise multiple lines. — (lower) The equivalent width (per pixel) spectrum. The smooth curves above and below the spectrum provide the $\pm 1\sigma$ and $\pm 5\sigma$ uncertainties. Regions meeting the condition given by Eq. 8.6 with $N_\sigma = 5$ are easily identified. The dotted vertical lines mark λ_- and λ_+ , the regions over which the feature equivalent widths are to be measured. Note that the region ends are defined where the equivalent width spectrum becomes consistent with the 1σ uncertainty.

The uncertainty in w_j is given by

$$\sigma_{w_j} = \frac{\Delta\lambda_j}{P^2} \left(\sum_{i=1}^M P_i^2 \sigma_{D,k}^2 \right)^{1/2}, \quad (8.16)$$

where

$$\sigma_{D,k}^2 = \left(\frac{\partial D_k}{\partial I_k} \right)^2 \sigma_{I_k}^2 + \left(\frac{\partial D_k}{\partial I_k^c} \right)^2 \sigma_{I_k^c}^2, \quad (8.17)$$

where σ_{I_k} is the uncertainty in I_k , and where $\sigma_{I_k^c}$ is the uncertainty in I_k^c . Written out, Eq. 8.17 is equivalent to Eq. 7.84. The σ_{w_j} serve as the 1σ equivalent width detection threshold at each pixel.

Objective line identification and equivalent width computations can then be performed in the identical manner outlined for the aperture method in Eqs. 8.3–8.8. Below, we describe the Gaussian fitting method for deter-

mining equivalent widths, line widths, line centroids, and their corresponding uncertainties. An additional benefit to fitting is that blended lines can be decomposed into individual Gaussian components.

8.1.1.3 Ionization Breaks

The most common ionization breaks in quasar spectra are due to neutral hydrogen ionization. The Lyman limit (LL) break has a rest-frame wavelength of 912 Å. It is measured from the optical depth at the Lyman ionization edge of neutral hydrogen,

$$\tau_{\text{LL}} = -\ln \left[\frac{F^{\text{L}}}{F^{\text{U}}} \right] \quad (8.18)$$

approaches or exceeds unity, where F^{L} is the mean counts averaged over a bin below the break, and F^{U} is the mean counts averaged over a bin above the break. Note that the definition does not use the normalized counts nor the fitted continuum. This is because fitting the continuum across a break is problematic.

Similar to the objective method of identifying absorption and emission features by computing an “equivalent width spectrum”, ionization breaks can be found by computing a “break index spectrum”. This method was also introduced by ?. The “break index” centered on pixel j is defined as

$$f_j = \frac{\langle F_j^{\text{L}} \rangle}{\langle F_j^{\text{U}} \rangle} = \frac{\left(\frac{1}{N_{\text{L}}} \right) \sum_{i=i_1}^{j-1} I_i}{\left(\frac{1}{N_{\text{U}}} \right) \sum_{i=j+1}^{i_2} I_i} \quad (8.19)$$

where $N_{\text{L}} = j - i_1$ and $N_{\text{U}} = i_2 - j$ are the number of pixels in the bins below and above pixel j , and pixel indices i_1 and i_2 are the upper and lower limits of the index range. Note that it is not required for N_{L} and N_{U} to be equal. The formalism allows for easy treatment of the spectrum edges, since the bins can be an arbitrary number of pixels. However, it is important that, as much as possible, the lower and upper bins remain constant in the rest frame. This is accomplished by defining the rest-frame lower limit λ_{L} and the rest-frame upper limit λ_{U} , from which the observed-frame limits,

$$\lambda_{i_1} = \lambda_{\text{L}} \left(\frac{\lambda_j}{\lambda_r} \right) \quad (8.20)$$

$$\lambda_{i_2} = \lambda_{\text{U}} \left(\frac{\lambda_j}{\lambda_r} \right), \quad (8.21)$$

are computed, where $\lambda_r = 912 \text{ \AA}$ for the Lyman ionization edge. Typical useful values for λ_L , and λ_U lie in the range $\pm 20\text{--}50 \text{ \AA}$ from 912 \AA .

The variance in f_j is

$$\sigma_{f_j}^2 = \frac{1}{\langle F_j^U \rangle} \left[\sigma_{F_j^L}^2 + f_j^2 \sigma_{F_j^U}^2 \right], \quad (8.22)$$

where

$$\sigma_{F_j^L}^2 = \frac{1}{N_L} \sum_{i=i_1}^{j-1} (I_i - \langle F_j^L \rangle)^2, \quad (8.23)$$

and

$$\sigma_{F_j^U}^2 = \frac{1}{N_U} \sum_{i=j+1}^{i_2} (I_i - \langle F_j^U \rangle)^2, \quad (8.24)$$

are computed directly from the counts in the spectrum.

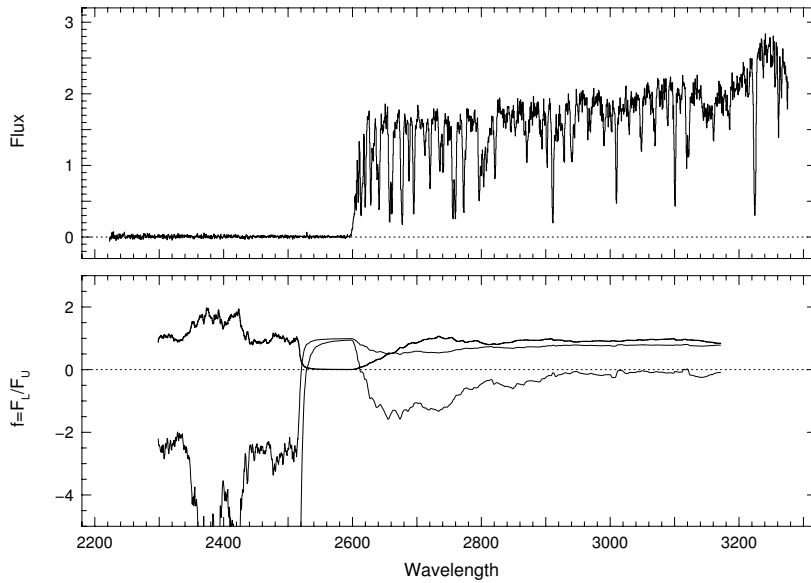


Figure 8.2: — (upper) An example quasar spectrum with a LLS. — (lower) The break index spectrum (thick curve) and the index sensitivity spectrum, $1 - N_\sigma \sigma_{f_\lambda}$, for $N_\sigma = 1$ (upper thin curve) and $N_\sigma = 5$ (lower thin curve). Note that the condition of Eq. 8.25 is met in the region of the LL break. Application of Eq. 8.26 locates the LLS at 2598.13 \AA , which is a redshift of $z = 1.48$. From Eq. 8.18, the optical depth for this break is $\tau_{LL} > 5.3$.

Using a significance criterion similar to that invoked for finding equivalent widths, candidate LL-breaks are identified at λ_j when the condition

$$f_j \leq 1 - N_\sigma \sigma_{f_j} \quad (8.25)$$

is met, where N_σ usually ranges between 3–5. The right hand side of Eq. 8.25 can be thought of as an break index sensitivity spectrum.

The redshift of the LLS is obtained by finding the location(s) in the spectrum where the difference between the break index sensitivity and the break index are a maximum,

$$\max(1 - N_\sigma \sigma_{f_j} - f_j). \quad (8.26)$$

The optical depth is computed from Eq. 8.18. In the case of an opaque break, the optical depth should be considered a lower limit.

The break index spectrum method is not as robust as the line finding methods presented above. For example, broad absorption line regions can masquerade as ionization breaks. It is useful to compute the break index spectrum for all observed wavelengths, including those redward of the $\text{Ly}\alpha$ emission line of the quasar. This provides additional insights into the identification of ionization break candidates.

8.1.2 Gaussian Profile Fitting

The equivalent widths of absorption lines can also be measured by modeling the line profile as a Gaussian function. This approach is appropriate when the resolution is low enough that the natural and thermal line broadening (the Voigt profile) are much narrower than the instrumental spread function, ISF. Furthermore, in the case of blended lines, multiple component Gaussian fitting can be used to deblend individual components.

The Gaussian function is written

$$G(\lambda) = D \exp \left[-\frac{1}{2} \left(\frac{\lambda - \lambda_c}{\Sigma} \right)^2 \right], \quad (8.27)$$

where λ_c is the central wavelength (at the line core), Σ is the line width (FWHM/2.35), and where D is the line depth. The flux at each wavelength across the profile is fitted using

$$\frac{I_\lambda}{I_\lambda^c} = 1 - G(\lambda), \quad (8.28)$$

where I_λ and I_λ^c are the counts in the spectrum and the fitted continuum at wavelength λ .

The goodness of the fit is usually determined by χ^2 minimization (see § 3.6). Minimization algorithms require an initial estimate of the parameters, in this case, D , Σ , and λ_c . These estimates can be obtained in an automated fashion directly from the data provided that each line has been found objectively (using the aperture or optimized approach), and the starting pixel, j_- , and ending pixel, j_+ , are known using the methods that apply to Eqs. 8.4 and 8.5. Very simplistic estimates are

$$\begin{aligned}\lambda_c &\simeq \frac{1}{2} (\lambda_{j_+} + \lambda_{j_-}) \\ D &\simeq 1 - \frac{I_{\lambda_c}}{I_{\lambda_c}^c} \\ \Sigma &\simeq \frac{1}{2.35} \max [\lambda_c/R, (\lambda_{j_+} - \lambda_{j_-})/2],\end{aligned}\tag{8.29}$$

where λ_c/R is the ISF FWHM and the factor of 2.35 is the conversion from FWHM to a Gaussian σ . The maximum function is invoked to insure that the line width is no smaller than the ISF. Physically, an absorption line cannot have a width narrower than the ISF width. However, noise in the data can have a realization that can, after χ^2 minimization, result in $\Sigma < \sigma_{\text{ISF}}$. In these cases, the Σ should be held at the ISF width, $\Sigma = \lambda_c/2.35R$. An illustration of Eq. 8.30 is presented in Fig. 8.3.

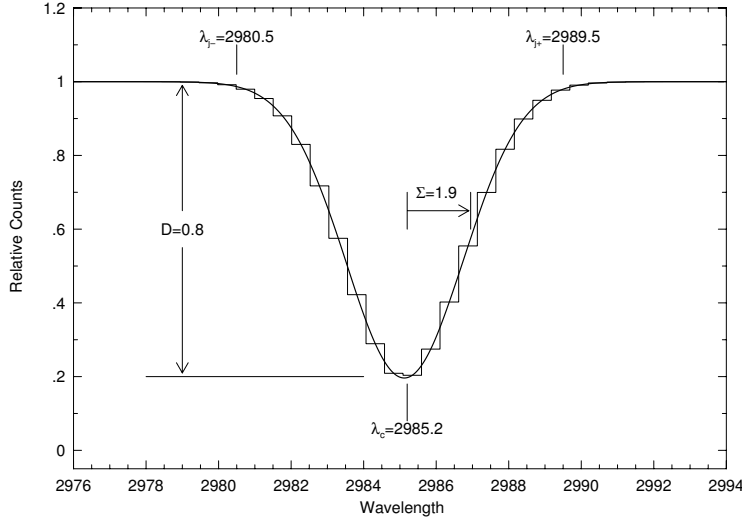


Figure 8.3: — An example of a Gaussian fit to a single absorption line. The initial estimate parameters, λ_c , D , and Σ (Eq. 8.30) are labeled, as are λ_{j_-} and λ_{j_+} . The solid lines is the fit after χ^2 minimization.

The observed equivalent width is obtained from the integral of $G(\lambda)$,

$$W = \int_{-\infty}^{\infty} G(\lambda) = \sqrt{2\pi} D \Sigma, \quad (8.30)$$

where the constant $\sqrt{2\pi}$ arises from the standard normalization of a unit-area Gaussian function.

Thus, there are three free parameters required to model an absorption line (λ_c, D, Σ) , of which the product $D\Sigma$ determines the observed equivalent width. The uncertainty in W , is given by

$$\sigma_W = \sqrt{2\pi} \left[(\Sigma\sigma_D)^2 + (D\sigma_\Sigma)^2 - (D\sigma_D)(\Sigma\sigma_\Sigma) \right]^{1/2}, \quad (8.31)$$

where the last term in Eq. 8.31 accounts for the anti-correlated errors in W (for a fixed W , the product $D\Sigma$ is a constant). Note that σ_W is independent of the uncertainty in the line center. Determination of the uncertainties in the fitting parameters is discussed in § 3.6. Note that even for an unresolved line, where Σ is held constant for the minimization, $\sigma_\Sigma \neq 0$. When computing the errors, the value of Σ should be treated as a free parameter.

8.1.2.1 Deblending Complex Lines

In the case of blended lines, multiple Gaussian functions can decompose the absorption profile as individual absorption lines, providing an equivalent width for each. The profile is modeled as

$$\frac{I_\lambda}{I_\lambda^c} = 1 - \sum_{i=1}^{N_{gp}} D_i \exp \left[-\frac{1}{2} \left(\frac{\lambda - \lambda_{c,i}}{\Sigma_i} \right)^2 \right], \quad (8.32)$$

where N_{gp} is the number of Gaussian components, and the D_i , $\lambda_{c,i}$, and Σ_i are the component line depths, central wavelengths, and widths. An example of deblending using multiple Gaussian functions is shown in Fig. 8.4.

The component equivalent widths and uncertainties are given by Eqs. 8.30 and 8.31, and the profile equivalent width and uncertainty are

$$W = \sum_{i=1}^{N_{gp}} W_i = \sqrt{2\pi} \sum_{i=1}^{N_{gp}} D_i \Sigma_i \quad (8.33)$$

and

$$\sigma_W^2 = \sum_{i=1}^{N_{gp}} \sigma_{W,i}^2, \quad (8.34)$$

respectively, where the σ_i are the component uncertainties given by Eq. 8.31.

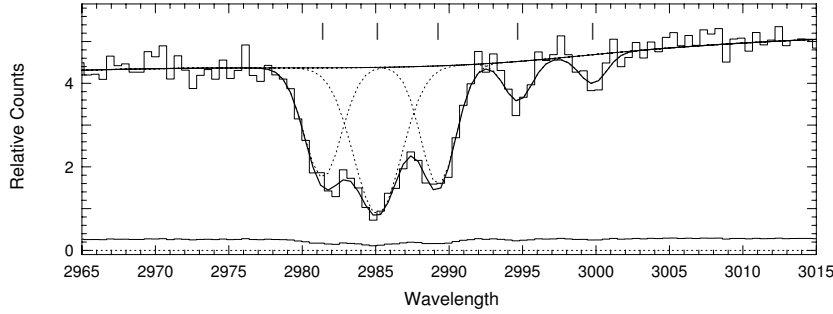


Figure 8.4: — An example of a blended Gaussian fit to five absorption lines. The three lines to the blue are resolved and deblended using the formalism of Eq. 8.32. The two lines to the red are unresolved, and the Gaussian widths, Σ have been fixed at the width of the instrument spread function.

8.2 Analysis of High Resolution Spectra

This material to be much further fleshed out.

High resolution quasar spectroscopy is necessary for resolving the profile shapes and exploring line of sight kinematics of multiple individual gas clouds. For the typical temperatures of individual absorbing gas clouds, the b parameters can range from a few to a few tens of kilometers per second. Thus, to infer the cloud temperatures and column densities of individual absorbing clouds, the quasar spectrum needs to be resolved on par with these narrow profiles.

Often, the relative line of sight velocities of the individual clouds are small enough that a complex absorption profile shape results. With high resolution spectra, the kinematics and column densities can be studied directly from the profile shapes as a function of velocity across the absorption system. In this chapter, we will describe these techniques, called the apparent flux decrement and apparent optical depth methods. A second method is Voigt profile decomposition, which is used to deblend the individual clouds and determine their velocities, column densities and b parameters. In cases where the velocity separations are greater than the cloud b parameters, multiple subsystems are observed within a system. In this chapter, we will also describe the practice of Voigt profile decomposition in some detail.

8.2.1 Velocity Resolution

It is useful to express the resolution of a spectrograph in terms of velocity. This provides the velocity width of an unresolved line and an observational lower limit to the gas temperature that can be inferred from the data.

Using the Doppler relation, the velocity resolution can be determined from

$$R = \frac{\lambda}{\Delta\lambda} = \frac{c}{\Delta v}, \quad (8.35)$$

where Δv is the FWHM velocity width of an unresolved absorption line. Thus, the velocity resolution is

$$\Delta v = \frac{c}{R} \quad \text{km s}^{-1}, \quad (8.36)$$

where the speed of light, c , is expressed in kilometers per second. A spectrograph with $R = 30,000$ has $\Delta v = 10 \text{ km s}^{-1}$. Note that the velocity resolution is independent of observed wavelength, and therefore absorber redshift.

To first approximation, the minimum b parameter, b_{min} , that can be measured for an unresolved line is simply Δv . From Eq. 5.60, this corresponds to an observable minimum temperature of

$$T_{min} = \left(\frac{m}{2K}\right) b_{min}^2 \simeq 6000 \left(\frac{m}{m_H}\right) \left(\frac{\Delta v}{10 \text{ km s}^{-1}}\right)^2 \quad (8.37)$$

where m/m_H is the ratio of the absorbing atomic mass to the mass of hydrogen. In terms of $R_{10} = R/10,000$, we have

$$T_{min} \simeq \frac{5.5 \times 10^4}{R_{10}^2} \left(\frac{m}{m_H}\right). \quad (8.38)$$

8.2.2 Kinematic Subsystems

Often the stronger member of a doublet is used as the “flag transition” from which many quantities that defined the kinematics and general characteristics of an absorption system are measured. Examples are the systemic redshift and the velocity range spanned by the absorbing gas.

Absorption features, whether weak and unresolved, or strong and kinematically complex, can be found using either the aperture or the optimized method presented in § 8.1.1. At high resolution, however, profiles often break up into separate “subsystems” that give the impression of being physically distinct gas complexes separated in line-of-sight velocity. These have been dubbed *kinematic subsystems*. Each kinematic subsystems

can be also be objectively defined using the formalism presented in § 8.1.1, with wavelength span bounded by λ_- and λ_+ .

For each kinematic subsystem, the full set of properties, including equivalent width, column density, velocity centroid, velocity width, can be measured directly from the data with no fitting or parametrized model. We will describe these measurements in the following subsections. In addition, the full system properties can be measured as well.

8.2.3 Apparent Flux Decrement and Optical Depth

The physical properties and kinematics of absorption can often characterized directly from the data. In practice, the data cannot be directly converted into the desired physical quantities. As we discussed in § 7.1.6, the resulting shapes of observed absorption profiles, I_λ , are not identical to the intrinsic line shape. Before the data are pixelized by the detector, the intrinsic line shape, $I_\lambda^c \exp(-\tau_\lambda)$, is compromised by the instrumental spread function, as written in Eq. 7.43,

$$I_\lambda = \Phi(\Delta\lambda) \otimes \{I_\lambda^c \exp[\tau_\lambda]\}, \quad (8.39)$$

where $\Phi(\Delta\lambda)$ is the ISF with FWHM equal to $\Delta\lambda$, and I_λ^c is the fitted continuum.

There are two useful approaches by which the profile kinematics can be directly measured from the data. The first is the apparent flux decrement (AFD), and the second is the apparent optical depth (AOD). Using the AFD quantifies each position along the profile in proportion to the radiative transfer equation post ISF convolution. The AOD quantifies each position along the profile directly in proportion to the column density post ISF convolution. In the case of $\tau_a(\lambda) \ll 1$, or in the case where virtually all pixels are saturated, the two methods are virtually identical.

8.2.3.1 Apparent Flux Decrement

The is the apparent flux decrement (AFD) of a pixel is defined as

$$D_a(\lambda) = 1 - I_\lambda/I_\lambda^c, \quad (8.40)$$

defined so that $0 \leq D_a(\lambda) \leq 1$. With high resolution spectra, resolved lines are often “black” in their cores, i.e., $I_\lambda \simeq 0$. In these cases, the saturated pixels often meet the condition

$$I_\lambda \leq \sigma_{I_\lambda}, \quad (8.41)$$

which actually yields an upper limit on the AFD,

$$D_a(\lambda) \geq 1 - \sigma_{I_\lambda}/I_\lambda^c \quad (8.42)$$

The AFD has many applications beyond those we will outline below. for example, the ADF distribution in the Ly α forest have been used to place constraints on the distribution of mass overdensities, $\Delta\rho/\langle\rho\rangle$.

8.2.3.2 Apparent Optical Depth

In principle, the run of optical depth across an absorption profile can be determined by inverting Eq 6.7, giving

$$\tau_\lambda = \ln \left(\frac{I_\lambda^c}{I_\lambda} \right). \quad (8.43)$$

where I_λ^c is the fitted continuum level. With high resolution spectra, resolved lines are often “black” in their cores, i.e., $I_\lambda = 0$. In these cases, the saturated pixels often meet the condition

$$I_\lambda \leq \sigma_{I_\lambda}, \quad (8.44)$$

and $\tau_a(\lambda)$ is a lower limit given by

$$\tau_a(\lambda) \geq \ln \left(\frac{I_\lambda^c}{\sigma_{I_\lambda}} \right). \quad (8.45)$$

8.2.4 Systemic Redshift

For most absorption systems, an *a priori* redshift is not determined. In such cases the systemic redshift, z_{abs} , is often defined subjectively by the observer. One objectively defined systemic redshift is the median of the AFD or AOD distribution of the flag transition, which is obtained by solving the implicit equation,

$$\int_{\lambda_-}^{\lambda_z} D_a(\lambda) d\lambda = \int_{\lambda_z}^{\lambda_+} D_a(\lambda) d\lambda, \quad (8.46)$$

or

$$\int_{\lambda_-}^{\lambda_z} \tau_a(\lambda) d\lambda = \int_{\lambda_z}^{\lambda_+} \tau_a(\lambda) d\lambda, \quad (8.47)$$

for λ_z , the observed wavelength at the ADF or AOD median, where λ_- and λ_+ are the extreme blueward and redward wavelengths of the overall absorption profile, respectively. This definition places the redshift at the

location where there is equal integrated AFD or AOD on either side of λ_z . In practice, it is useful to set $D_a(\lambda) = 0$ or $\tau_a(\lambda) = 0$ whenever $I_\lambda + \sigma_{I_\lambda} \geq I_\lambda^c$, which avoids unphysical AFD and AOD values.

The systemic redshift is then

$$z_{abs} = \frac{\lambda_z}{\lambda_o} - 1, \quad (8.48)$$

where λ_o is the rest-frame wavelength of the flag transition.

8.2.5 Absorber Velocities

Once z_{abs} is determined, the observed wavelength scale of absorption profiles associated with the system can be converted to rest-frame velocities using the Doppler relation,

$$v_{sys} = c \left(\frac{\lambda - \lambda_z}{\lambda_z} \right) \quad (8.49)$$

assuming $v \ll c$. For each kinematic subsystem, the velocity extremes are defined in the same way,

$$v_- = c \left(\frac{\lambda_- - \lambda_z}{\lambda_z} \right) \quad (8.50)$$

$$v_+ = c \left(\frac{\lambda_+ - \lambda_z}{\lambda_z} \right), \quad (8.51)$$

where λ_- and λ_+ are the extreme blueward and redward wavelengths of each kinematic subsystem.

Having transformed the profiles to rest-frame velocity, the absorption kinematics can now be quantified.

8.2.5.1 Mean Velocities

By definition of z_{abs} , the velocity of the full systems has $v = 0$. However, each individual kinematic subsystem has a non-zero mean velocity, $\langle v \rangle$. As with the absorber systemic redshifts, we compute the mean velocities from either the AFD or AOD distribution of the flag transition absorption profile. The mean velocity for a kinematic subsystem is the first velocity moment computed over the velocity range of the subsystem. In terms of the AOD distribution,

$$\langle v \rangle = \frac{1}{\tau_a} \int_{v_-}^{v_+} \tau_a(v) v dv, \quad (8.52)$$

where v , v_- , and v_+ are defined in Eqs. 8.49, 8.50, and 8.51, respectively, and

$$\tau_a = \int_{v_-}^{v_+} \tau_a(v) dv. \quad (8.53)$$

The mean AOD velocities are only sensical if z_{abs} was computed using Eq. 8.47. Note that, if using the ADF weighted scheme (Eq. 8.46), then Eq. 8.52 should also be computed in terms of the AFD by substituting $D_a(\lambda)$ in place of $\tau_a(\lambda)$

8.2.5.2 Velocity Widths

The velocity width of a kinematic subsystem, ω_v , is defined by the second moment of the apparent optical depth,

$$\omega_v^2 = \frac{1}{\tau_a} \int_{v_-}^{v_+} \tau_a(v) [v - \langle v \rangle]^2 dv \quad (8.54)$$

This quantity is the equivalent Gaussian width of the optical depth profile.

As with the mean AOD velocities, the AOD velocity widths are only sensical if z_{abs} was computed using Eq. 8.47. If using the ADF weighted scheme (Eq. 8.46), then Eq. 8.54 should also be computed in terms of the AFD.

8.2.6 AOD Column Densities

The AOD column density method is effectively a pixel by pixel conversion of $\tau_a(v)dv$ to $N_a(v)dv$, where $N_a(v)$ is the column density in the interval $v \rightarrow v + dv$ and is defined per unit velocity [$\text{atoms cm}^{-2} (\text{km s}^{-1})^{-1}$], and where dv is the velocity width of a single pixel in the rest-frame of the absorption system.

From the definition of $\tau_\lambda = N\alpha(\lambda)$, we can write the total column density per unit velocity as

$$N_a(v)dv = \frac{mc}{\pi e^2} \frac{1}{f\lambda} \tau_a(v)dv, \quad (8.55)$$

where $dv = (c/\lambda)d\lambda$, and the apparent optical depth is given by Eq. 8.43.

The integrated apparent column density of a system or kinematic subsystem is given by

$$N_a = \int_{v_-}^{v_+} N_a(v)dv, \quad (8.56)$$

where v_- and v_+ are the velocity extrema of the system or kinematic subsystem being measured. It is convenient to quote $N_a(v)$ in logarithmic units,

$$\log N_a(v) = \log \tau_a(v) - \log f\lambda + 14.576, \quad (8.57)$$

where the fundamental physical constants are assumed to have negligible uncertainty.

8.2.6.1 AOD Doublet Method: Unresolved Saturation

The $N_a(v)$ profiles of doublets, or other same-ion transitions having $f\lambda$ differing by a factor of two, can be used to discern the velocity location of unresolved saturation in absorption profiles.

Savage & Sembach have shown that this technique yields accurate column densities when the width of the instrumental spread function does not exceed the *intrinsic* line widths by more than a factor of a few. No corrections [also see Jenkins (1997)] have been applied to the measured $N_a(v)$.

8.2.7 Voigt Profile Decomposition

Voigt profile (VP) decomposition is an established technique for modeling complex and blended absorption profiles because it is well suited for parameterizing the absorbing gas properties into physically meaningful quantities, i.e., the number of components (clouds), their line-of-sight velocities, column densities, and Doppler b parameters.

Recall that when an absorption line having optical depth $\tau_\lambda = N\alpha(\lambda)$ is recorded by an instrument having an ISF function $\Phi(\Delta\lambda)$, the measured spectrum is the convolution of the intrinsic spectrum and the ISF,

$$I_\lambda = \Phi(\Delta\lambda) \otimes \{I_\lambda^c \exp[-N\alpha(\lambda)]\}, \quad (8.58)$$

where $I^c(\lambda)$ is the fitted continuum, and I_λ is the observed intensity profile due to absorption and smearing from the ISF.

From Eq. 5.56, the optical depth due to a single isothermal cloud is

$$\tau_\lambda = N\alpha(\lambda) = \frac{\sqrt{\pi}e^2}{mc^2} \frac{Nf\lambda^2}{\Delta\lambda_D} H(x, y), \quad (8.59)$$

where $H(x, y)$ is the Hjerting function given by Eq. 5.57, evaluated at

$$x(\lambda, \lambda_c, \Delta\lambda_D) = \frac{\lambda - \lambda_c}{\Delta\lambda_D} \quad (8.60)$$

where the Doppler width, $\Delta\lambda_D$, is given by Eq. 5.43. We have generalized the definition of x from Eq. 5.58 to account for an observed line center, λ_c , that may be offset due to a line-of-sight velocity shift from λ_z (the observed wavelength of the systemic redshift). The Hjerting function is also evaluated at

$$y(\Delta\lambda_D) = \frac{\lambda^2 \Gamma}{4\pi c} \frac{1}{\Delta\lambda_D}, \quad (8.61)$$

where Γ is the transition damping constant.

Thus, for each VP, there are three free parameters, N , λ_c , and $\Delta\lambda_D$. The column density N appears Eq. 8.59 as a proportionality between τ_λ and $\alpha(\lambda)$. The line center, λ_c , appears in the quantity x , which is employed in the evaluation of the Hjerting function. It is $\Delta\lambda_D$ that appears in three locations: the denominator of Eq. 8.59, and the denominators of x and y (Eqs. 8.60 and 8.61) appearing in $H(x, y)$. As given by Eq. 8.60, the Doppler b parameter is simply

$$b = \frac{c}{\lambda} \Delta\lambda_D = \left(\frac{2kT}{m} \right)^{1/2} \quad (8.62)$$

When an absorption profile is a complex blend of several clouds with different line of sight velocities, it can be treated as a composite of multiple Voigt profiles. Then the optical depth used in Equation 8.58 is the sum of the individual cloud optical depths,

$$\tau_\lambda = \sum_{k=1}^{N_{vp}} \tau_{\lambda,k} \quad (8.63)$$

where each $\tau_{\lambda,k}$ is given by Equation 8.59, and the total number of free parameters becomes $3N_{vp}$.

Invoking the property that

$$\exp\left(\sum x_k\right) = \prod \exp(x_k) \quad (8.64)$$

the VP decomposition of a profile can be described by a single function of the form

$$I_\lambda = \Phi(\Delta\lambda) \otimes \left\{ \prod_{k=1}^{N_{vp}} \exp[-\tau_{\lambda,k}(\lambda_c, N, b)] \right\}, \quad (8.65)$$

where the $\tau_{\lambda,k}$ are given by Eq. 8.59. VP decomposition usually involves a χ^2 minimization between the model I_λ and the observed profile. We will discuss the practice of VP decomposition in a later chapter.

It is very important to know the shape and the width of the ISF profile for VP decomposition. Inferring the number of “clouds” in a kinematically complex profile, and measuring their column densities, N , and b parameters is very sensitive to the ISF profile shape and width. Having too wide a profile can result in too few clouds being inferred and an N distribution that would likely be skewed toward larger column densities. On the otherhand, the b parameters would be overestimated, which, because N and b are anticorrelated for a fixed equivalent width, the N of the incorrectly inferred clouds would be underestimated.

8.2.8 Pixel Statistics Methods

Not yet written.

